Pure Appl. Geophys. 183 (2026), 2697–2713
© 2026 The Author(s), under exclusive licence to Springer Nature Switzerland AG, modified publication 2026
https://doi.org/10.1007/s00024-026-03937-w

Pure and Applied Geophysics

Challenges to Ten Common Views in Earthquake Source and Ground Motions—a Review

Igor A. Beresnev[1]

Abstract—Evidence has accumulated over time against the correctness of certain existing concepts in understanding earthquake source and ground motions. They pertain to: the parameters that can be realistically resolved from seismic spectra, the reality of earthquake scaling, the true sources of short-period radiation, the reasons for the unexplained suppression of high frequencies in recorded motions, the applicability of point-source models, or the definition of the seismic near field. The alternative views on these subjects can be addressed in a non-contradictory manner from a single unifying platform. Such a paradigm views the earthquake rupture as one fundamentally controlled by two independent parameters, the static slip and the slip velocity, each respectively defining the low- and high-frequency ends of the radiation spectrum. It also considers the earthquake source as fundamentally having a finite size that cannot be neglected even for the smallest events of practical interest.

Keywords: Earthquake source, Strong ground motions, Fault slip, Fault-slip velocity, Finite faults, Earthquake radiation.

1. Introduction

Certain concepts persist in the earthquake-source science, as well as in the simulations and interpretation of strong ground motions, despite the growing evidence challenging their correctness. The facts, criticisms, and alternative views have been scattered through the literature and are not easy to find in a concentrated form. It is the viewpoint of the author that a review would be timely to summarize the challenges to several common notions (stopping short of terming them "misconceptions") in one critical digest, primarily directed toward newcomers. Such a review would re-formulate the difficulties with the existing paradigm and call attention to the reasons underlying them, in the hope that the summary would stimulate progress toward the correct models. Providing such a review is the purpose of this paper.

In the following, we will consider ten relevant topics, approached one-by-one. None of the criticisms are in themselves new, as it should be in a review; in all cases, appropriate (but not exhaustive) references are given. According to the purpose, we point out the perceived difficulty, provide a quantitative rationale, and propose a corrected alternative if it is possible. We admit that not everyone may share our views, in which case our conclusions are open to debate and a counter-argument if it exists.

2. Concepts Challenged

2.1. Concept 1: Rupture Size can be Inferred from the Corner Frequency of Radiated Spectrum

Several widely used concepts are based on a certain assumption about the form of the Fourier amplitude spectrum of seismic waves at long distances. Perhaps the most popular is the ω-square model of the source spectrum introduced by Aki (1967, his Eq. 30). For a point source and a shear wave, the far-field amplitude spectrum of wave displacement at distance R is postulated to have the form

$$u(\omega) = \frac{M_0}{4\pi\rho\beta^3 R}\frac{1}{1+(\omega/\omega_c)^2}, \qquad (1)$$

where M_0 is the moment, ρ is the density, and β is the shear-wave velocity (e. g., Boore, 1983, his Eqs. 1–3). The quantity ω_c is the corner frequency. The

[1] Department of the Earth, Atmosphere, and Climate, Iowa State University, 253 Science I, 2237 Osborn Drive, Ames, IA 50011-3212, USA. E-mail: beresnev@iastate.edu

physical meaning of this parameter can be established based on the temporal form of the earthquake slip that radiates the spectrum defined by Eq. (1):

$$\Delta u(t) = U\left[1 - \left(1 + \frac{t}{\tau}\right)e^{-t/\tau}\right] \equiv U\Delta u_s(t), \qquad (2)$$

where U is the final slip, $\Delta u_s(t)$ is the shape factor, and $\tau \equiv 1/\omega_c$ (Beresnev & Atkinson, 1997, their Eq. 6). The slip in Eq. (2) starts at zero and gradually approaches the constant level U.

The quantity τ (and thus ω_c) in Eq. (2) is the characteristic time scale. If one defines the rise time T as the period over which the slip reaches a fraction x of U, then, for given x, T can be found as the root of the equation $\left[1 - (1 + t/\tau)e^{-t/\tau}\right] = x$. For example, for x = 0.95 and 0.99, the roots T/τ are 4.74 and 6.64, respectively. However, such a specific relationship is ambiguous due to the freedom in how x is chosen.

Another assumption is needed to express the rise time through the characteristic fault dimension L. A common-sense proposition is that a point slips as long as the rupture propagates across the fault, leading to $T = L/(y\beta)$, where the rupture-propagation speed is taken as a fraction y of the shear-wave velocity. One observes, though, that the validity of any specific form of this relationship would be questionable, not only because of the wide range possible for y, but also because it does not account for the geometry of the fault, position of the hypocenter, possible local healing, or changes in rupture velocity. Then equating the two definitions of T gives a tentative relationship between the corner frequency and L. If, for example, a trial value of 0.8 for y is assumed, $\omega_c = 3.8\beta/L$ and $\omega_c = 5.3\beta/L$ for the two respective choices of x.

Brune (1971), based on a different argument, proposed the classic formula $\omega_c = 2.34\beta/L$. Variants of this relationship are still widely used (e. g., Kaneko & Shearer, 2014, their Eq. 2; Shearer, 2019, his Eq. 9.47; Bindi et al., 2021, their Eq. 7; Parolai, 2023, his Eq. 8; Koper et al., 2024, their Eq. 1; Allen, 2025, his Eq. 6; Baltay et al., 2025, their Eq. 1; Bindi et al., 2025, their Eq. 1; Kurzon et al., 2025, their Eq. 5; Zuo et al., 2025, their Eq. 2). Here we emphasize that such a relation derives from arbitrary choices and cannot be expected to lead to a reliable determination of the fault size, in view of a large and generally unknown uncertainty in its numerical coefficient (that can be denoted as K).

2.2. *Concept 2: Tectonic-Stress Drop Controls the Strength of High-Frequency Radiation*

At high frequencies ($\omega \gg \omega_c$), the spectrum in Eq. (1) becomes

$$u_{hf}(\omega) = \frac{M_0}{4\pi\rho\beta^3 R\omega^2}\omega_c^2, \qquad (3)$$

or it is proportional to the square of the corner frequency. Stress drop $\Delta\sigma$ is a commonly used parameter in the simulations of strong ground motions that is responsible for the high-frequency spectral levels, thus controlling the peak velocities and accelerations as factors of engineering significance. To express $u_{hf}(\omega)$ through $\Delta\sigma$, a link between the latter and ω_c is needed.

In providing the link, one typically begins with the definition of the stress drop as

$$\Delta\sigma = \frac{C\mu U}{L}, \qquad (4)$$

where μ is the shear modulus and $C \approx 1$ (Kanamori & Anderson, 1975, their Eq. 1). This formula follows, for example, from the analytical solution for the maximum relative displacement of the faces of a thin hollow spheroidal cavity in an elastic medium for the case of Poisson's ratio of ¼ (Eshelby, 1957; Beresnev, 2001, his Eq. 17). Then Eq. (4), together with $\omega_c = K\beta/L$ and the definition of the seismic moment, lead to

$$\omega_c = K\beta\left(\frac{\Delta\sigma}{M_0}\right)^{1/3} \qquad (5)$$

and, upon substitution into Eq. (3), to the well-known formula

$$u_{hf}(\omega) = \frac{K^2 M_0^{1/3}}{4\pi\rho\beta R\omega^2}\Delta\sigma^{2/3} \qquad (6)$$

(C has been assumed to equal 1).

This result implies that, for given moment, the high-frequency spectrum scales with a power of $\Delta\sigma$, thus suggesting that larger relief in tectonic stress creates greater amplitudes of short-period radiation. Such a conclusion does not seem to be correct even

on intuitive grounds. Indeed, same tectonic stress may be released in a conventional ("fast") earthquake or in a slow creep-like event. Clearly, the former case will produce strong short-period radiation whereas the latter will create none. Therefore, there is difficulty in interpreting the quantity $\Delta\sigma$ in Eq. (6) as the real change in the stress during earthquakes.

In finding the root of the contradiction, one should compare the physical problem leading to Eq. (4) with the one describing an earthquake source. The former considers the stress displacing the faces of a pre-existing cavity by U in its center relative to each other in purely elastic deformation. The latter deals with the stress change during the creation of a crack of same length and same displacement when energy is spent on breaking the continuity of the solid. These are two different physical problems, and the stress changes in the two cases cannot be expected to be equal. This circumstance prevents the usage of Eq. (6) for the determination of stress change in seismic events based on observation of wave spectra.

A non-contradictory alternative formulation of Eq. (6) is obtained by invoking the maximum velocity $v_{\max}$ at which the faces of the fault slip. This velocity is obtained by taking the derivative of Eq. (2), which has the maximum at $t = \tau$:

$$v_{\max} = \frac{U}{e\tau} = \frac{U\omega_c}{e}. \tag{7}$$

Through $v_{\max}$, Eq. (3) is re-written as

$$u_{hf}(\omega) = \frac{M_0 e^2}{4\pi\rho\beta^3 R U^2 \omega^2} v_{\max}^2 = \frac{A e^2}{4\pi\beta R U \omega^2} v_{\max}^2, \tag{8}$$

where A is the fault area. This equation does correctly explain why "fast" earthquakes (large $v_{\max}$) produce intense seismic radiation while the slow ones are only felt in the long-period range.

Beresnev (2024) showed that the factor $v_{\max}^2/U$, seen in Eq. (8), invariably comes out in spectral and temporal measures of high-frequency radiation from various popular source time functions. The control of the peak slip velocity over the short-period levels appears to be universal and independent of the particular form of reasonably defined earthquake slip.

2.3. *Concept 3: One-Parameter Scaling of Earthquake Spectrum Exists*

The concept of scaling is based on the idea that the entire source spectrum can be expressed as a function of only one parameter, e. g., the earthquake magnitude (Aki, 1967; Boore, 2003, his Fig. 2; Bindi et al., 2025, p. 2857). For example, if ω_c in Eq. (1) obeys Eq. (5), and the quantity $\Delta\sigma$ in the latter can be assumed constant, then the only remaining controlling parameter is the seismic moment M_0. This concept is known as the constant-stress-drop scaling. The idea is appealing, as only one parameter is needed to describe the spectrum at both low and high ends.

In assessing the viability of such a hypothesis, we first note the absence of a clear physical reason why $\Delta\sigma$, defined in Eq. (4) by the ratio of fault displacement to its dimension, should necessarily stay constant in nature. Second, the low- and high-frequency bands of the seismic spectra are controlled by different physical quantities. As follows from Eq. (1), at low frequencies ($\omega \ll \omega_c$) the controlling parameter is solely the seismic moment (or magnitude), through the displacement U. At high frequencies (Eq. 8), these are both the moment and the peak slip rate $v_{\max}$, the latter being a much stronger factor due to its square power. The need for two independent parameters to explain the full seismic spectrum thus has fundamental physical underpinnings. The static displacement, expressed in the value of seismic moment, is only responsible for the low-frequency asymptote. On the other hand, the high-frequency content (Eq. 8) depends on how fast the fault slips. If only U were in control of high-frequency radiation, this would imply the existence of a functional relationship $U(v_{\max})$; however, there is no evidence for the existence of such a law: the final displacement cannot in itself unambiguously determine how fast it has been achieved. The physical considerations suggest that U and $v_{\max}$ should be fully independent, each controlling its respective part of the spectrum, foreclosing the possibility of a one-parameter scaling.

2.4. *Concept 4: High-Frequency Radiation is Generated During Sudden Movements of Rupture*

A view is often found that high-frequency radiation forms when ruptures experience "jerky" motion (Madariaga, 1977, 1983; Somerville et al., 1999, p. 60; Shi & Day, 2013). The validity of this assumption can be put to a direct test by comparing the spectra from crack propagation with constant and variable speeds. A convenient and rigorous simulation tool is the source-representation integral (Aki & Richards, 1980, their Eq. 14.37; Beresnev, 2017b, his Eq. 1).

The problem is formulated as follows (Beresnev, 2026). The calculations are performed for a 3400 × 3400 m strike-slip fault, approximately corresponding to a M_w 5 earthquake, with the constant offset $U = 0.14$ m and the omega-square slip function. The peak slip rate $v_{\max}$ is set to 0.25 m/s. The hypocenter is placed in the center of the fault. The local radial rupture speed is randomized around the constant value of 0.8β as $0.8\beta(1+\eta)$. The random variable η is drawn from the normal distribution with zero mean and the desired standard deviation, constrained to equal -0.9 if it accidentally fell below or was equal to -1. If the speed exceeded 1.5β, it was kept at 1.5β, allowing local supershear propagation.

Three values of standard deviation in η were tested: 0.1, 0.2, and 0.3. The resulting rupture fronts are depicted in Figs. 1a-c. For comparison, the undisturbed radial propagation with constant speed of 0.8β was also considered.

The spectrum of the fault-normal component of the full seismic field was computed by the numerical integration of the Fourier transformation of the representation integral (Beresnev, 2024, his Eq. 3). The observation point was placed in the direction of the upper edge of the fault, coinciding with the x_1 axis, at the distance of 10,000 m from the nearest edge, thus having the coordinates {3400 + 10,000, 0, 0} m (the coordinate system is shown in Fig. 1 of Beresnev, 2017a). The amplitude spectra of particle displacement for all four scenarios are presented in Fig. 2. They show that the spectra from uneven ruptures, despite the degree of their front complexity, are indistinguishable, except random scatter, from the rupture propagation with the constant speed. The absence of preferential production of high frequencies by irregular cracks can be understood on physical grounds. Selective boost of energy in certain frequency bands in a kinematic model can only be achieved through the effects of regular interference, arising from the coherent summation of radiation with different timing from various parts of the fault. Constructive/destructive interference can boost or suppress spectral amplitudes for ordered rupture travel, but such deterministic effects cannot be

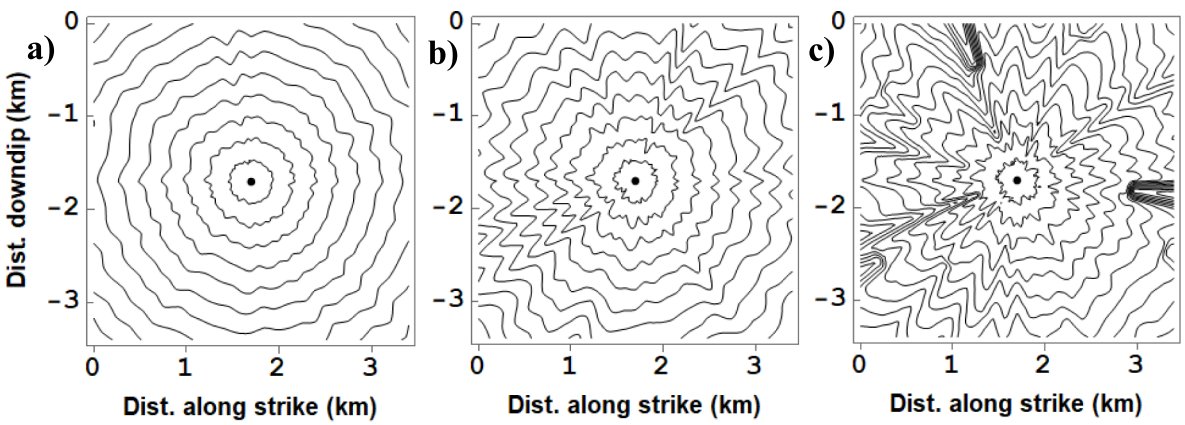


Figure 1
a–c Simulated irregular rupture fronts corresponding to standard deviations in η of 0.1, 0.2, and 0.3, respectively. The isochrones are spaced at 0.1 s

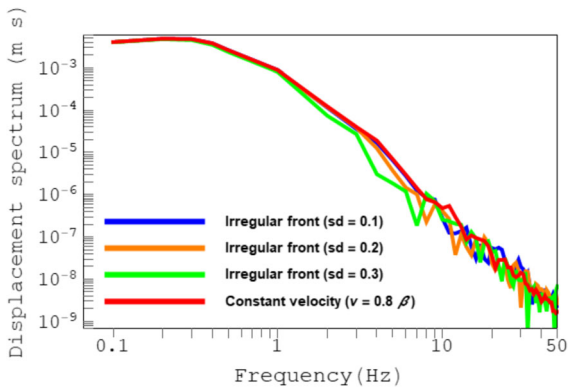


Figure 2
Fourier amplitude spectra of ground displacement for the geometrically irregular anisotropic rupture fronts and the constant-speed radial front with the same average velocity. The color version of this figure is available only in the electronic edition

significantly disrupted by chaotic movements around the same average speed of rupture propagation. Randomization of rupture timing does not appreciably change the spectral content of radiation, as long as the same average velocity is preserved.

2.5. *Concept 5: Small-Scale Fault Heterogeneity (Asperities) is the Source of High-Frequency Ground Motions*

Another commonly presumed source of high-frequency radiation is the small-scale heterogeneity of slip. This idea forms the basis for the assumption that heterogeneous slip distributions can be resolved from the inversions of ground-velocity or acceleration records.

The representation integral can again be used to verify the validity of this concept. We place the observation point in the near field at 200 m above the upper corner of the fault and offset by 200 m in the direction x_2 perpendicular to the fault plane, thus having the coordinates of {0, 200, 200} m. Sufficiently heterogenous slip distributions impose limitations on the convergence of the integral; for that reason, the calculations are performed for a smaller 1200 × 1200 m fault with $U = 0.035$ m, corresponding to a M_w 4 earthquake. The hypocenter is placed in the middle of the edge of the fault opposite to the observation point, with the coordinates of {0, 0, –600} m. The rupture propagation is thus unilateral toward the station, corresponding to the strongest directivity pulse. The front travel is radial with the constant speed of 0.8β.

The slip follows the k-square model, where k is the wavenumber, as used by Beresnev (2024), with the fault discretization of 200 samples per length and width, giving the spatial sampling interval of 1200/199 ≈ 6 m. Slips following the k-square decay are often employed in the synthetic rupture generators for seismic-hazard computations (Herrero & Bernard, 1994; Somerville et al., 1999, pp. 75–76; Mai & Beroza, 2002; Gallovič & Brokešová, 2004; Graves & Pitarka, 2010, p. 2096; Schmedes et al., 2013, p. 1121; Infantino et al., 2020, pp. 2563–2564; Rodgers et al., 2020, p. 2866). The omega-square source time function is still used, and the corner frequency can be calculated from Eq. (7) as

$$\omega_c = \frac{e v_{\max}}{U(\xi)}, \tag{9}$$

where ξ is the position on the fault plane and $v_{\max}$ is kept at 0.25 m/s. The corner frequency is now variable over the fault, with the average of $f_c = e \times 0.25/(2\pi \times 0.035) = 3.1$ Hz. The spectrum is again calculated by the numerical integration for the fault-normal radiation component.

Thirty different realizations of the k^{-2} slip were generated: an example is provided in Fig. 3 (Beresnev, 2024, his Fig. 5). All distributions have the same fault-average value of $U = 0.035$ m. Figure 4 shows

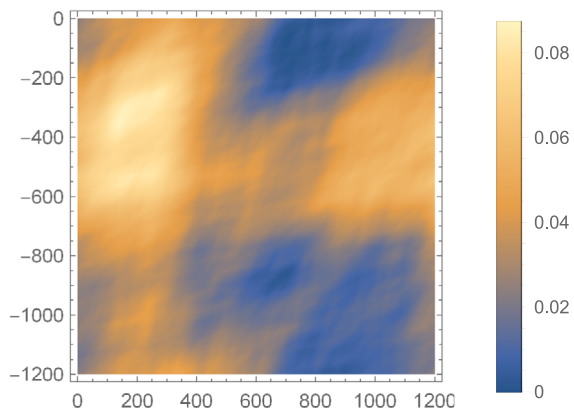


Figure 3
An example realization of k^{-2} heterogeneous slip. The scale is slip in m. The color version of this figure is available only in the electronic edition

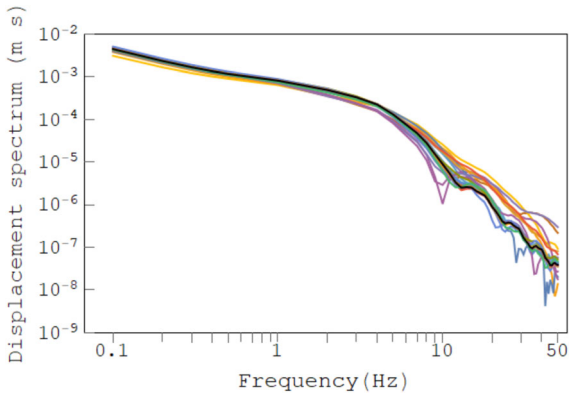


Figure 4
Fourier spectra of ground displacement from thirty heterogeneous ruptures (colored lines) and the uniform fault with the same average slip (black line). The color version of this figure is available only in the electronic edition

the spectra of radiation from all these models, separated by different colors. For comparison, the spectrum from the uniform fault with same constant slip and same $v_{\max}$ is presented by the black line.

Inspection of Fig. 4 shows that, out of the thirty spectra from inhomogeneous faults, only seven are conspicuously above the case of the uniform rupture (the black line). Twenty-two cluster around the latter with approximately same slope, and one lies below. The conclusion that fault heterogeneity (the presence of asperities) necessarily leads to the production of high frequencies (selectively boosting the short-period content and thus decreasing the overall spectral slope) does not hold true. Such a behavior, too, can be understood on physical grounds. For the uniform-slip case, the corner frequency of radiation from all parts of the fault is the same, and a particular spectral slope forms as a result of regular interference of delayed radiation. On the other hand, when the corner frequency is allowed to vary randomly across the fault, as in all other cases, the resulting spectral slope becomes the result of incoherent summation of radiation from various parts having various corner frequencies, generally leading to different spectral decays from realization to realization.

2.6. *Concept 6: Slip Distributions with k^{-2} Spatial Spectra Emit Radiation with ω^{-2} Frequency Spectra*

The next concept is the notion that, if earthquake slip follows the k-square wavenumber spectrum, the frequency spectrum of radiation has the omega-square shape (Somerville et al., 1999, p. 76; Mai & Beroza, 2002, p. 10–1). This result can be traced back to the work of Herrero and Bernard (1994, their Eq. 24), expressing the body-wave displacement spectrum in the far field of a linear rupture propagating along the ξ_1-axis as

$$u(\omega) = FU\left[\omega\left(\frac{1}{v} - \frac{\cos\Psi}{\beta}\right)\right], \qquad (10)$$

where $U(k_1)$ is the one-dimensional spatial Fourier transform of the slip distribution $U(\xi_1)$, v is the rupture speed, Ψ is the angle between the ξ_1-axis and the direction to the receiver, and F is an unspecified dimensional coefficient. The result was obtained for the slip-velocity function represented as the delta function. For this case, it is true that, if $U(k_1)$ has the k-square shape, then $u(\omega)$ acquires the same shape when $\omega(1/v - \cos\Psi/\beta)$ is substituted for k_1.

Beresnev (2022, his Eq. 9) noted that the same result for any form of the slip-velocity function, restricted to the case when $\Delta u_s(t)$ does not depend on the position on the fault (constant τ in case of the omega-square source in Eq. 2), follows in the same approximation of a small near-linear source in the far field from the representation integral (Aki & Richards, 1980, their Eq. 14.18),

$$u(\omega) = const\,\Delta\dot{u}_s(\omega)U\left[\omega\left(\frac{\cos\Psi}{\beta} - \frac{1}{v}\right)\right], \qquad (11)$$

where $\Delta\dot{u}_s(\omega)$ is the spectrum of the slip-velocity function, and the exact value of the dimensional coefficient *const* is omitted for brevity. Equation (11) shows that, unlike the particular case of Eq. (10), the seismic-wave spectrum in the general instance is additionally multiplied by the spectrum of the slip-velocity function. If $U(k_1)$ is k^{-2}, and if $\Delta\dot{u}_s(\omega)$ is ω^{-2}, then the resulting spectrum of radiation decays as ω^{-4}.

Equation (11) is valid for the case of the slip function of uniform shape, in which the parameter τ

(and thus the corner frequency) is identical at all points on the fault. On the other hand, we have already seen in Fig. 4 that the spectral roll-offs should be expected to vary if the corner frequency is allowed to spatially fluctuate. To observe how the asymptotic behavior in Eq. (11) changes if the narrow source has heterogeneous slip, we compute the exact field numerically from the representation integral. The fault has the length L = 3400 m. The k^{-2} slip with the omega-square source time function is generated as in the example of Figs. 3 and 4, with the discretization of 100 samples per L, $v_{\max}$ equal to 1 m/s, and the average offset of 0.14 m, keeping the average corner frequency at 3.1 Hz. To satisfy the narrow-source condition $W << L$, the width W is set to 5 × L/99 m. The placement of the hypocenter is as in the example of Figs. 3 and 4.

To remain in the same approximation under which Eq. (11) was derived, the small-source condition (Aki & Richards, 1980, their Eq. 14.12) has to be satisfied. Accordingly, the coordinates of the observation point were arbitrarily set to $\{10^4, 0, 0\}$ km. The specific distance value does not carry particular significance: it appears as a multiplier in the constant term in Eq. (11) and in this approximation merely serves as a scaling factor.

Figure 5 presents the seismic spectra from thirty different realizations of k-square slip. They are seen to form a cloud diverging toward the high-frequency end. The two straight gray lines show the high-frequency slopes visually fitted to the end-member possibilities in the diverging "conical" area: their fall-off rates (the powers of frequency) are –2.9 and –3.6. The other cases are intermediate to these. The meaning of the dotted black line is discussed later in the text. Figure 5 demonstrates that, as long as the corner frequency of the source time function is allowed to vary, the k-square distributions generate a variety of spectral slopes in the resulting radiation, all of them being greater than –2. Similar variability in the near field was demonstrated in Fig. 4. The slope takes on the maximum steepness of –4 when the corner frequency of the omega-square slip function is constant along the entire narrow fault, as in the asymptotic case of Eq. (11).

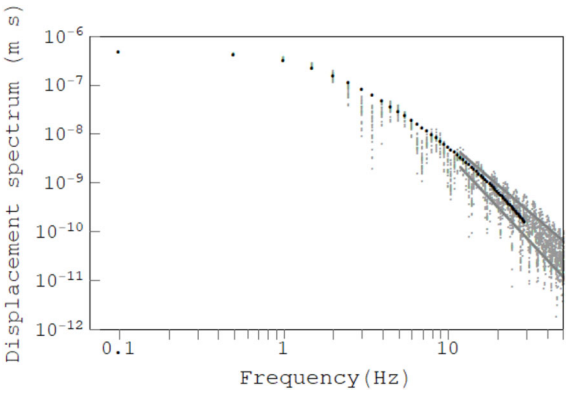


Figure 5
Fourier spectra of ground displacement from thirty heterogeneous ruptures on a narrow finite fault. The straight lines bracket the scatter of possible high-frequency spectral slopes. The black dotted line is the spectrum of the equivalent omega-square point source ($v_{\max}$ = 0.5 m/s) with the kappa operator applied (κ = 0.025 s)

2.7. *Concept 7: The "Kappa" Filter is Caused by Near-Surface Attenuation*

Both Eq. (11) and Fig. 5 demonstrate that fault finiteness contributes an additional decay to the radiated spectrum compared to the slope expected from an omega-square point source alone (Eq. 1). Observations show that seismic spectra are devoid of high-frequency content and cannot be explained by the pure omega-square radiation corrected for path attenuation (Anderson & Hough, 1984): to match them, simulated ground motions need to be additionally low-pass-filtered by applying a suppressing exponential operator $\exp(-\pi\kappa f)$, where κ is a fitting parameter. Such an artificially introduced suppression is known as the kappa filter (Boore, 2003, his Eq. 20; Ktenidou et al., 2014). The exact nature of this effect is still debated; most often, it is attributed to the near-surface attenuation unaccounted for by the regular anelastic Q along the propagation path. For example, Parolai (2018) proposes to explain the kappa filtering by scattering on near-surface heterogeneities. The study (Parolai, 2018, his Fig. 5) documents a steady decrease in the quality factor due to scattering as randomness in near-surface layering increases, although it does not quantify whether the resulting extra decay is in the range of the typical values of specifically the parameter κ. There also are opinions that kappa is "*an empirical parameter*" "*not measuring any specific physical phenomenon*", arising

from "*great simplifications of complex source, path, and site effects*" (Palmer & Atkinson, 2023, pp. 2666–2667). We could paraphrase this statement as "*kappa is a formal parameter accounting for all phenomena going beyond the omega-square radiation corrected by the path Q*".

Beresnev (2023a, 2024, 2025, 2026) proposed that the observed extra diminution of high-frequency energy be rather explained by an alternative form of the source time function and/or the fault finiteness itself, that is, by purely the source effect. As an example, the black dotted line in Fig. 5 represents the spectrum radiated by an omega-square point source in Eq. (1) with the exactly same moment as that of the narrow finite fault at the same distance, multiplied by $\exp(-\pi\kappa f)$, fitted with $v_{\max} = 0.5$ m/s and $\kappa = 0.025$ s. The fitting with κ was carried out to the frequency of 30 Hz, as typically done in the recent empirical determinations of this parameter (Nye et al., 2023, their figs. 2 and 3). The equivalent κ is well within the empirical range of this parameter: for example, most values reported by Nye et al., (2023, caption to their Fig. 4) fall between 0.028 and 0.045 s. We note that the high-frequency slopes seen between the straight lines are fully due to the finite-fault effects, without any additional filtering. To explain the same slopes by the point-source model, the kappa operator has to be applied.

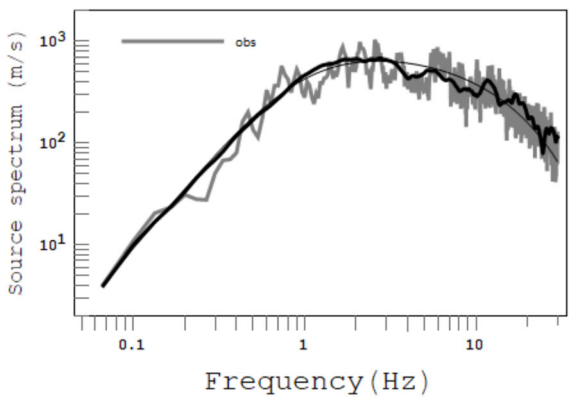


Figure 6
Source acceleration spectra for the M 5.1 6 February 2015 earthquake in Japan. The average observed spectrum is shown by the gray line. The thin and thick black lines represent the point-source simulation of the same event with the kappa operator applied and its finite-fault simulation without this operator, respectively

The equivalence between the finite-fault radiation and that from a kappa-filtered point source is further corroborated in Fig. 6. To quantify the departure of the source spectrum radiated by a finite fault from the omega-square shape (Eq. 1), we divide the former by the latter at all frequencies. Such a ratio was termed the "finite-fault correction" by Beresnev (2023a). Beresnev (2023a, his Fig. 3) calculated the finite-fault correction for eight rupture scenarios on a M 5 earthquake fault: it has the shape of a high-cut filter. The gray line in Fig. 6 displays the path-corrected average source acceleration spectrum of the M 5.1 6 February 2015 earthquake recorded by the KiK-net network in Japan (Beresnev, 2023a, his figs. 6 and 7). The thick black line is the simulated finite-fault spectrum, obtained by multiplying the omega-square shape by the finite-fault correction and fitted to the observation by varying the parameter $v_{\max}$, equal to 0.9 m/s in this case. No kappa operator was used. The thin black line is the omega-square spectrum multiplied by the kappa filter: in this case, $v_{\max} = 0.36$ m/s and $\kappa = 0.028$ s. The black curves are virtually identical, showing the equivalence between the kappa filtering and the finite-fault effect in explaining the same high-frequency content. In addition, the point-source simulation is unrealistically smooth: it lacks the irregularities present in both the finite-fault simulation and the observed data.

Putting the reason for the observed diminution of high-frequency spectra to the earthquake source itself

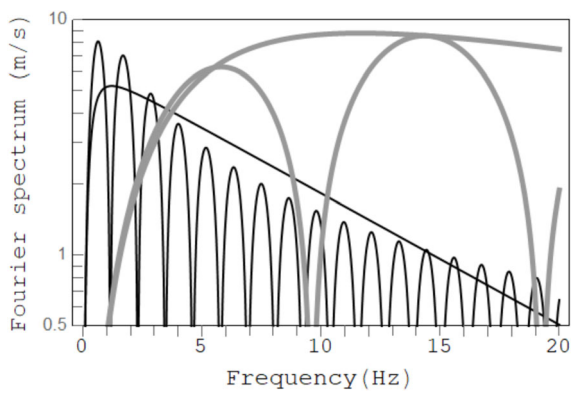


Figure 7
Source acceleration spectra for the Haskell rupture for a M 6 (black line) and M 4 (gray line) earthquakes. Also shown are the point-source simulations of the same spectra with the kappa operator applied

naturally resolves the difficulties typically encountered in attributing it to local-site response. First, negative kappa values have been reported, that is, the existence of the acceleration spectra that are not attenuated but rather amplified at high frequencies, relative to the flat omega-square shape (Haendel et al., 2023, their figs. 4, 6, 7, 8, 10; Palmer & Atkinson, 2023, their Table 2). An increase in acceleration spectra with frequency appears natural if a slip-velocity function with the spectral fall-off rate less than ω^{-2} is invoked. For example, Beresnev (2023a, his Table 2) deduced the slopes of the spectra of this function ranging from ω^{-1} to ω^{-3} from the analysis of all well-recorded earthquakes by the KiK-net in the magnitude range from 4 to 6.

Second, there has been persistently documented poor correlation between the κ value and the physical characteristics of the site, including its average shear-wave velocity (Ktenidou et al., 2014, their Fig. 2; Haendel et al., 2023, their figs. 7 and 8; Palmer & Atkinson, 2023, their Fig. 16). If one assumes that the high-frequency decay is controlled by the source instead, such a correlation should not be expected.

Third, significantly different κ 's are inferred from earthquake data for the western (WNA) and eastern/central (ENA) North America. For example, Boore and Joyner (1997) deduced a generic $\kappa = 0.035$ s for an M_w 6.5 earthquake on rock in WNA; their fitting range was to 20 Hz. On the other hand, a much lower $\kappa = 0.006$ s is generally accepted for ENA (Toro et al., 1997, p. 43). It should be noted in this regard that a substantive difference between the two respective regional databases is that the ENA historic seismicity is much scarcer and consists primarily of small-magnitude events. For example, the EPRI ground-motion database, from which the ENA value was derived, consists of the recordings of 66 events with the average magnitude of 3.6 (Electric Power Research Institute, 1993, their Table 2.A-1). A more recent database contains 92 events with the average magnitude of 4.3 (Goulet et al., 2021, their Table 1). According to Eq. (9), such events will exhibit much higher corner frequencies than their large-magnitude counterparts, obscuring the identification of the true high-frequency spectral decay and causing the underestimation of kappa.

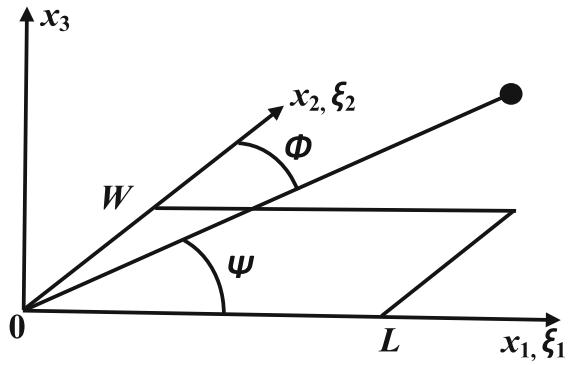


Figure 8
Geometry of radiation from a rectangular finite fault

We illustrate the latter point using the same model that led to the radiated spectrum in Eq. (11). For a unidirectional rupture and constant static offset U across the entire fault (the Haskell solution), the spatial spectrum in Eq. (11) reduces to the sinc function, leading, for the omega-square slip, to the modulus of the radiated frequency spectrum from the finite fault as

$$u(\omega) = \frac{M_0}{4\pi\rho\beta^3 R} \frac{1}{1 + (\omega/\omega_c)^2} \left| \frac{\sin X}{X} \right|, \qquad (12)$$

where $X = (\omega L/2)[1/v - (\cos\Psi)/\beta]$ [Aki & Richards, 1980, their Eq. 14.18; the authors omit the dimensional coefficient in front of the solution (12), which we have retained for completeness]. One sees (cf. Equation 1) that the difference with the point-source radiation is that the omega-square spectrum here is multiplied by the sinc function, the latter serving as the finite-fault correction for the Haskell rupture. The correction is equivalent in this case to the kappa operator. To illustrate the differences for two dissimilar magnitudes, Fig. 7 presents the finite-fault spectra, calculated from Eq. (12), for $M = 6$ and 4. The spectra were computed at the same reference distance of 1 m. In calculating the seismic moments, the respective characteristic fault lengths were taken as 10,000 and 1200 m, and, to remain within the near-line-source approximation, the width was taken as 10 m. The constant slips were 0.49 and 0.035 m, $v_{\max}$ in Eq. (9) was 1 m/s, $v = 0.8\beta$, and $\Psi = 0$ (the forward-directivity case). The corner frequencies, calculated from Eq. (9), are 0.88 and 12 Hz. The peaks and troughs in the spectral shapes in Fig. 7

correspond to the instances of regular interference owing to the orderly rupture propagation.

Similarly to Figs. 5 and 6, the point-source omega-square spectra with the same moments as those of the finite faults in Eq. (12), multiplied by the kappa operator and visually fitted to the finite-fault shapes, are also shown, the fitting parameters being $v_{\max} = 0.4$ m/s, $\kappa = 0.041$ s and $v_{\max} = 0.5$ m/s, $\kappa = 0.012$ s for the M 6 and 4 events, respectively. Note that the true high-frequency decay in the frequency ranges much exceeding the corner frequencies would be ω^{-3} in either case: it is magnitude-independent. However, the kappa values recovered if the finite-fault spectrum is interpreted through a filtered point-source model (0.041 and 0.012 s) are substantially different, being an artifact of the limited frequency range of the fitting (same as in Boore & Joyner, 1997) and the much higher corner frequency of the M 4 event. These kappa values are very close to the averages adopted for the western and eastern North America. The dependence of the inferred values of kappa on the frequency band in which it is measured was earlier noted by Parolai and Bindi (2004). As one can see, the artifact causes the apparent magnitude dependence of kappa. Also note that the true $v_{\max}$ of 1 m/s, used to produce the finite-fault spectra, is recovered incorrectly in both cases if the point-source model with kappa is used to interpret the spectra.

Fourth, individual sites exhibit high variability in their κ values measured from different events (Nye et al., 2023, their Fig. 4b; Haendel et al., 2023, p. 2659). Again, such a scatter is naturally explained if it is attributed to the variations in the parameters of the earthquake sources used to measure the site-specific value.

The following related test can be conducted. If the observed decay is truly a site-specific parameter, locations with identical site conditions will exhibit the same kappa values for the same earthquake source. Beresnev (2026) calculated the ground-acceleration spectra from the rupture model presented in Fig. 1b, at three observations sites that are distinctly different geometrically but all correspond to the original elastic-space formulation of the problem and thus have no site response. In addition to the far-field station with the coordinates {3400 + 10,000, 0, 0} m (same as in Fig. 2), two additional near-field stations, situated at the opposite ends of the fault, were added, with the coordinates {0, 200, 200} m and {3400 + 200, 0, 0} m. The spectra at all three stations were fitted with the kappa-filtered equivalent point source as in Figs. 5 and 6. The resulting kappa values were 0.013, 0.004, and 0.025 s, respectively. Note that these values are all realistic and distinctly different. In real world, they could be erroneously interpreted as "site-specific", while they are due entirely to the direction-dependent finite-source effect that forms a particular slope, not to variations in site conditions.

The same purely directional effect on kappa is observed in the behavior of the finite-fault correction. We have seen that this correction for the case of a far field of a small narrow Haskell rupture reduces to a sinc function (Eq. 12). The same form of the representation theorem that leads to this model can be used to extend it to the more general situation of a small rectangular source, in which the width is independent of the length. In this case, the double integration in Eq. (14.16) of Aki and Richards (1980) replaces the spectrum in the authors' Eq. (14.18) with

$$u(\omega) = \omega \Delta u_s(\omega) WL \frac{\sin X}{X} \frac{\sin Y}{Y} \left[\exp i \left(\frac{\omega r_0}{\beta} - \frac{\pi}{2} + X - Y \right) \right], \tag{13}$$

where r_0 is the distance from the origin to the observation point (Aki & Richards, 1980, their Fig. 14.1), $Y = (\omega W/2)\cos\Phi/\beta$, and Φ is the angle between the ξ_2-axis and the direction to the receiver (the ξ_2-axis is in the fault plane perpendicular to ξ_1: Aki & Richards, 1980, their Fig. 14.2; see also Fig. 8). Equation (12) then is replaced with

$$u(\omega) = \frac{M_0}{4\pi\rho\beta^3 R} \frac{1}{1 + (\omega/\omega_c)^2} \left| \frac{\sin X}{X} \frac{\sin Y}{Y} \right|. \tag{14}$$

One can see that, for the rectangular rupture, the finite-fault correction is the product of two sinc functions. Unlike the one in Eq. (12), the frequency slope of the product (and thus of the low-pass filter that it represents) is variable: it changes from ω^{-2} to ω^{-1} (e. g., at $\Phi = 90°$). These variations are controlled by the angle Φ but not the fault dimensions L and W: that is, they are magnitude-independent. Independence of the observed behavior of kappa on

magnitude has been reported in the literature (e. g,, Nye et al., 2023, p. 824).

We can illustrate the angular variability in the high-frequency behavior for $\Psi = 90°$ (radiation in the plane perpendicular to the fault). Figure 9 presents the rectangular-fault correction $\left|\frac{\sin X}{X}\frac{\sin Y}{Y}\right|$ for the limiting cases of $\Phi = 0$ (black line) and 90° (gray line) (radiation along the ξ_2-axis and in the direction perpendicular to the fault, respectively). The fault is a square, with L and W equal to 3400 m and $v = 0.8\beta$. To reduce the quasi-periodic spectral oscillations due to regular interference, the curves were discretized into 400 intervals in the 0–30 Hz range shown and smoothed by a seven-point running average. This time, we measure the equivalent value of kappa in the traditional way by fitting the negative high-frequency slope with the function $A_0\exp(-\pi\kappa f)$ on log-linear axes, where A_0 is an adjustable constant that on these axes moves the fitting line up and down (Anderson & Hough, 1984, their Eq. 1; Nye et al., 2023, their Eq. 1). The typical fitting interval is 5 to 30 Hz (Nye et al., 2023, their Fig. 2). The values of κ of the visually matched straight lines in Fig. 9 are 0.044 and 0.020 s for $\Phi = 0$ and 90°, respectively. Again, this variation is well within the observed empirical range of this parameter.

The directional effect on the equivalent kappa decay will be quantitatively similar in both the situations of multiple events recorded by a single station and multiple stations recording a single event. In either case, the variability in the inferred kappa will be purely a source-directivity phenomenon, unrelated to the conditions at any particular site. Indeed, the scatter in the inferred kappa values obtained for various earthquakes at given site, on one hand, and among different sites for one given event, on the other, is quantitatively similar (cf. Figures 9 and 11 of Anderson & Hough, 1984). This fact is readily understood if the scatter in both cases has the same underlying cause.

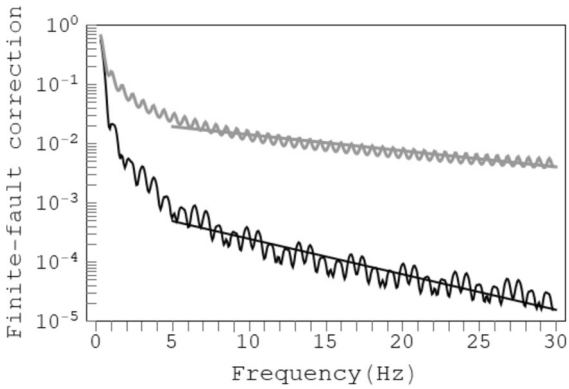


Figure 9
Finite-fault correction for a square fault, corresponding to $M = 5$, for two perpendicular radiation directions. The black and gray lines: $\Phi = 0$ and 90°, respectively. Also shown are the straight lines fitted to the high-frequency slopes and used to measure the respective values of kappa

The finite-fault corrections always carry the shape of a high-cut filter, as, for example, is seen in the modulation of the source spectrum by the sinc functions in Eqs. (12) and (14). An example of such a shape is given in Fig. 9. This is explained by the interference of the waves emanating from different parts of the fault, which add up exactly in-phase at the very long periods only. To produce the high-frequency suppression, always present in the radiation from finite sources, in their simulations by point sources, an artificial kappa operator has to be introduced as a proxy for the finite-fault interference effect. Accounting for fault finiteness removes the need for such an ad-hoc filtering.

Studies, in which the finite-fault radiation is simulated deterministically at low but stochastically at high frequencies (Aagaard et al., 2010; Graves & Pitarka, 2010), still use, despite employing the actual fault geometry, the kappa operator to reduce the high-frequency amplitudes. The reason is that, in the stochastic method, due to the difficulties in the fully deterministic computation, the short-period radiation is simulated through the summation of the omega-square spectra from subfaults represented as point sources. Such a summation tends to preserve the underlying shape of the point-source spectra; in addition, their random phasing does not produce the correct spectral slope that would be created by deterministic interference of waves emitted from a continuous fault plane.

The results reviewed do not prove that a contribution to kappa decay cannot arise from the local site geology. However, they do demonstrate that the typically observed kappa values and variability can be fully accounted for by the effects arising at the source, including the finite rupture dimensions and

directivity. The specific form of rupture travel, the variations in slip distribution, fault shape, hypocenter position, or the shape of the source time function all lead to the apparent κ filtering (Beresnev, 2023a, 2024, 2025, 2026).

2.8. *Concept 8: Moderate-Magnitude Events can be Simulated as Point Sources*

A relevant question to ask is what is the size of the rupture that can then be safely simulated as a point source not requiring any high-frequency modification? It follows that, for that fault, the finite-fault correction should equal one in the entire frequency range of practical interest.

We can evaluate such a condition by considering the finite-fault correction $|\sin X/X|$ for the same model of Haskell rupture: it is reproduced in Fig. 10 for an M 4 earthquake with the same parameters as in Fig. 7. The correction is reasonably close to unity only at the frequencies up to approximately 5 Hz, above which it precipitously drops. It follows that satisfactory modeling of an event even as small as M 4 should account for their finite size. If earthquakes of this size and greater are treated as point sources, the models will necessarily require a kappa filter, introduced in an ad-hoc manner to explain the realistic shape of the finite-fault spectra at the frequencies above 5 Hz. This limiting frequency becomes progressively lower as the magnitude increases (e. g., Beresnev, 2023a, his Fig. 9), further restricting the ability to model larger earthquakes as point sources.

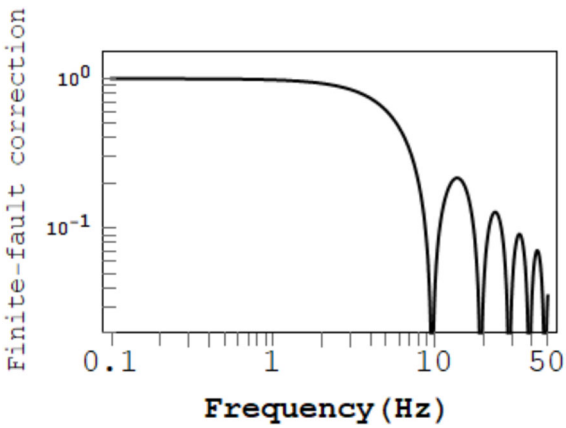


Figure 10
Finite-fault correction for the Haskell rupture corresponding to $M = 4$

2.9. *Concept 9: Distribution of Total Slip on the Fault can be Recovered from Ground-Motion Records*

We have seen (concept # 3) that the frequency content of radiation above the corner frequency is fundamentally controlled by two parameters: U and $v_{\max}$, the latter carrying the dominant influence. If one uses such a higher-frequency band to solve solely for U, as is done in the approach known as the linear matrix inversion (Hartzell & Heaton, 1983; Hartzell & Helmberger, 1982; Heaton, 1982), errors will occur, because, in this band, the two parameters strongly trade-off with each other. Inversions of strong-motion records for distributions of static slip on causative faults of significant earthquakes, with magnitudes greater than six, using this method have been routinely performed all over the world (e. g., Mendoza et al., 2024; Ye et al., 2016). Such inversions will inevitably be prone to errors if they utilize the data beyond the characteristic corner frequency of the event (Beresnev, 2023b).

As an example, consider a M 7 earthquake. As illustrated by the simplified models of Eqs. (11) and (12), the corner frequencies are imposed by the source time function. For a typical offset of $U = 2$ m and $v_{\max} = 1$ m/s, the corner frequency is estimated from Eq. (9) as $f_c = e \times 1/(2\pi \times 2) = 0.2$ Hz. To remain within the validity of the one-parameter assumption, the frequencies of the data would need to remain below this limit; however, linear inversions of strong ground motions have often not followed this restriction (Beresnev, 2003, pp. 2452–2454). In this case, a certain value of slip velocity is always implicitly assumed. For instance, isosceles triangles have been widely utilized to represent the slip-velocity function in the inversion algorithms. Then the set base (duration) of the triangle becomes the proxy for the slip velocity (see Eq. 17). The amount of its trade-offs with the resolved static slip and the resulting error usually remain unknown.

Nonlinear inversions, based on the minimization of an objective function, which simultaneously solve for more than one parameter of faulting, remove the

severe restriction on the frequency band. However, the trade-offs between the resolved parameters remain significant. For example, the algorithm of Ji et al. (2002) searches the parameter space for the values of four variables: the slip magnitude, slip duration, rake angle on the fault, and rupture speed. The slip-velocity function is taken in the form of a cosine:

$$\dot{u}(t) = U\frac{1-\cos(2\pi t/T)}{T}, 0 \le t \le T, \qquad (15)$$

where T is the duration (rise time) (Ji et al., 2002, their Eq. 2). The ground-motion records that typically are used in strong-motion inversions are ground velocities, whose shape is controlled by the second derivative of $u(t)$:

$$\ddot{u}(t) = 2\pi\frac{U}{T^2}\sin\left(2\pi\frac{t}{T}\right). \qquad (16)$$

Even though the algorithm independently solves for both U and T, Eq. (16) demonstrates that the amplitude of the ground-velocity is controlled by the ratio U/T^2: small changes in T will result in significant alterations in the resolved slip U. For both the cosine slip in Eq. (15) and the triangular function, the duration is the proxy for the slip velocity through the same formula

$$T = \frac{2U}{v_{\max}}. \qquad (17)$$

Equation (16) thus precludes an unambiguous determination of both U and T. The resulting uncertainties in the inverted images are often not quantified. To quote from Mai et al., (2016, p. 691), who present a candid view of the ability of various inversion algorithms to recover the true dynamics of faulting: "*rigorous uncertainty quantification in earthquake source studies is needed but, unfortunately, is often neglected.*"

2.10. *Concept 10: The Extent of the Near Field of an Earthquake is Controlled by the Seismic Wavelength*

Mathematical description and modeling of the seismic near field is much more involved compared to the sufficiently long distances, making it important to have the rigorous definition of the transition between the two zones. The distinction is conveniently made through the comparison of various terms in the representation integral.

The commonly found near-field condition, $R \ll \lambda$, where λ is the wavelength, is formulated in the frequency domain and is based on the direct comparison of complex-number terms in the integrand of the Fourier transform of the representation integral (e. g., Aki & Richards, 1980, p. 88). However, such a comparison is only mathematically allowed for real numbers. As a consequence, a paradoxical result is obtained: the near field extends to infinity at near-zero frequencies (e. g., for the static displacement). If this were the case, permanent ground displacement would dominate the shape of the seismic-displacement pulse at any distances from an earthquake; however, this is only observed very near the faults.

An alternative, non-contradictory near-field condition can be derived from the time-domain form of the representation integral, where the terms in the integrand are allowed to be directly compared (Beresnev, 2025). Beresnev (2017b, his Eq. 1) provided such a form convenient for the analysis (for brevity, we do not reproduce it here). Using a comparison property of integrals (e. g., Stewart, 1999, p. 333), we first estimate the value of the leading near-field term (first term in the integrand):

$$\begin{aligned}
&\left(1/R^4\right)\int_{R/\alpha}^{R/\beta} t'\Delta u(\xi, t-t')dt' \le \left(1/R^4\right)\\
&(R/\beta - R/\alpha)\max[t'\Delta u(\xi, t-t')]_{\text{from } R/\alpha \text{ to } R/\beta}\\
&\qquad \le \left(1/R^4\right)(R/\beta - R/\alpha)(R/\beta)\\
&U = \left(1/R^2\right)(1/\beta - 1/\alpha)(U/\beta)
\end{aligned}$$

(α is the P-wave velocity). We then estimate at what distances this term dominates over the far-field ones. The near-field condition for the first term relative to the fifth becomes: term1/term5 $\approx \left[\left(1/R^2\right)(1/\beta - 1/\alpha)(U/\beta)\right]/\left[v_{\max}/\left(\beta^3 R\right)\right] = (1-\beta/\alpha)(U/R)(\beta/v_{\max}) \gg 1$. For Poisson's solid, $\beta/\alpha = 1/\sqrt{3} \approx 0.6$. Except for the small correction by the factor $(1-\beta/\alpha)$, the near-field condition by-order-of-magnitude follows as

$$R \ll U\frac{\beta}{v_{\max}} \qquad (18)$$

[we follow the common rule in the asymptotic assessment of mathematical orders of magnitude, in which the constants of proportionality are not included—e. g., Van Dyke (1964, p. 25)].

The condition expressed by Eq. (18) is physically meaningful. If slip velocity $v_{\max}$ becomes very small, the near-field term dominates to very long distances, resulting in no conventional wave propagation in the form of seismic pulses and the static displacement extending far from the fault. Also, recall that $v_{\max}$ controls the strength of the high-frequency radiation. Therefore, if $v_{\max}$ is large, the near-field terms are insignificant everywhere, and conventional high-frequency seismic pulses with no permanent displacement dominate. The observational analogs of these two end-member cases are slow earthquakes (tremor) vs. conventional earthquakes.

Consider again an example of a M 7 earthquake (U = 2 m, $v_{\max}$ = 1 m/s). For the shear-wave velocity of 3000 m/s, the criterion in Eq. (18) yields $R << 6$ km. This is the estimation of the characteristic range of distances at which significant permanent displacement should be observed. To compare, the largest geodetically measured ground displacement around the fault of the M_w 7.2 Landers, California earthquake occurred within approximately 10 km from the rupture (Wald & Heaton, 1994, their Fig. 4). Note, in this regard, that the maximum near-surface slip U in this event was inferred to be close to 6 m (Wald & Heaton, 1994, their Fig. 14), which would shift the estimate of the extent of the near field further upward, possibly by a factor of three. For greater events, the extent of the near-field zone will scale with their size according to the increasing value of their average slip U (Eq. 18).

3. *Concluding Remarks*

Most of the inferences in this review have been obtained from considering a model of seismic dislocation as one controlled by two independent physical parameters, the final slip and the velocity at which it has been achieved (the slip rate over the rise time of the event). Both are important to invoke to explain the spectral content of wave radiation at the low- and high-frequency ends; the separating corner frequency is defined by the same two parameters. Important conclusions can in addition be derived from asymptotic models of a small narrow and a small rectangular sources in the far field, for which the complicated wave field simplifies to a physically transparent form and even allows analytical solutions. Unlike the popular point-source approximation, these models correctly incorporate the fault finiteness, the latter playing a crucial role in explaining the observed radiation features. The conclusions naturally following from such simplified models are corroborated by the numerical simulations from the exact representation integral of elasticity.

Approaches, using formal fitting parameters to describe earthquake ground motions, are well established. For example, the "stress parameter" $\Delta\sigma$ is a standard tunable quantity in the stochastic simulations used to control the short-period spectral levels (e. g., Boore, 1983, p. 1868; Atkinson & Beresnev, 1997), while the parameter κ is tuned to artificially introduce a decay in such spectra that otherwise would be unphysically flat. Large numbers of empirical determinations of such fitting parameters and their variability have been made. Although, as this review demonstrates, they are shown to be proxies for real physical quantities (the peak slip rate and fault finiteness, respectively), the approaches seem to satisfy the practical purposes of seismic-hazard calculations. What is then an advantage of switching to the alternative real physical variables? In our view, the advantage is not as practical as methodological. It spells the difference between empiricism and physics-based modeling. Empiricism, widely used in earthquake engineering, codifies what it cannot explain, but the ultimate goal of scientific inquiry is to understand, explain, and predict natural phenomena. The advantage of our models is that they deduce the same phenomena from the laws of physics; unlike empirical relationships, they have the power to explain and predict.

As an example, modeling earthquakes as sources of finite dimensions naturally introduces the necessary high-frequency decay of the radiated spectra, without resorting to the need to measure an additional empirical parameter. If one insists that it be measured and ascribed to the effect of the local site condition, its value will acquire additional uncertainties caused,

for example, by the unfavorable signal-to-noise ratio, ambiguous identification of the shear-wave window, or soil-structure interaction in the instrument installation. The latter effect takes place in the frequency range in which κ is measured (Castellaro et al., 2022; Hollender et al., 2020). All these factors make measured value of the empirical parameter kappa even less reliable.

Acknowledgements

The author is grateful to V. Graizer for the helpful comments and suggestions.

Author Contribution There is only one author.

Data Availability

No external data were used in the paper. All inferences were made through the analyses of the respective equations and literature sources as indicated.

Declarations

Conflict of interest The authors declare no competing interests.

Publisher's Note Springer Nature remains neutral with regard to jurisdictional claims in published maps and institutional affiliations.

Springer Nature or its licensor (e.g. a society or other partner) holds exclusive rights to this article under a publishing agreement with the author(s) or other rightsholder(s); author self-archiving of the accepted manuscript version of this article is solely governed by the terms of such publishing agreement and applicable law.

References

Aagaard, B. T., Graves, R. W., Rodgers, A., Brocher, T. M., Simpson, R. W., Dreger, D., Petersson, N. A., Larsen, S. C., Ma, S., & Jachens, R. C. (2010). Ground-motion modeling of Hayward fault scenario earthquakes, Part II: Simulation of long-period and broadband ground motions. *Bulletin of the Seismological Society of America, 100*, 2945–2977.

Aki, K., & P. G. Richards. (1980). *Quantitative Seismology*, W. H. Freeman and Company: San Francisco.

Aki, K. (1967). Scaling law of seismic spectrum. *Journal of Geophysical Research, 72*, 1217–1231.

Allen, T. I. (2025). Systematic estimation of earthquake source parameters for continental Australia: Attenuation and stress drop. *Bulletin of the Seismological Society of America, 115*, 2671–2689.

Anderson, J., & Hough, S. (1984). A model for the shape of the Fourier amplitude spectrum of acceleration at high frequencies. *Bulletin of the Seismological Society of America, 74*, 1969–1993.

Atkinson, G. M., & Beresnev, I. A. (1997). Don't call it stress drop. *Seismological Research Letters, 68*, 3–4.

Baltay, A., Abercrombie, R. E., Oth, A., & Uchide, T. (2025). Introduction to the special section on improving measurements of earthquake source parameters. *Bulletin of the Seismological Society of America, 115*, 723–733.

Beresnev, I. A. (2026). *Spectral behavior of seismic radiation from irregular rupture fronts* (in review).

Beresnev, I. A. (2001). What we can and cannot learn about earthquake sources from the spectra of seismic waves. *Bulletin of the Seismological Society of America, 91*, 397–400.

Beresnev, I. A. (2003). Uncertainties in finite-fault slip inversions: To what extent to believe? (A critical review). *Bulletin of the Seismological Society of America, 93*, 2445–2458.

Beresnev, I. A. (2017a). Factors controlling high-frequency radiation from extended ruptures. *Journal of Seismology, 21*, 1277–1284.

Beresnev, I. A. (2017b). Simulation of near-fault high-frequency ground motions from the representation theorem, *Pure Appl. Geophys., 174*, 4021–4034.

Beresnev, I. A. (2022). Spatial heterogeneity of fault slip and the radiated spectra of ground motions. *Bulletin of the Seismological Society of America, 112*, 1463–1471.

Beresnev, I. A. (2023a). A method to simulate high-frequency decay of acceleration spectra of ground motions without the need of kappa or f_{max} filters. *Bulletin of the Seismological Society of America, 113*, 1115–1132.

Beresnev, I. A. (2023b). Uncertainties in finite-fault slip inversions, Part II: Fault discretization and parameterization of slip function, *Pure Appl. Geophys., 180*, 59–68.

Beresnev, I. A. (2024). Physical characteristics controlling radiation from heterogeneous ruptures – finite faults. *Bulletin of the Seismological Society of America, 114*, 2869–2885.

Beresnev, I. A. (2025). The applicability of point-source models in ground-motion prediction, *Pure Appl. Geophys., 182*, 45–53.

Beresnev, I. A., & Atkinson, G. M. (1997). Modeling finite-fault radiation from the ω^n spectrum. *Bulletin of the Seismological Society of America, 93*, 67–84.

Bindi, D., Oth, A., Parolai, S., Picozzi, M., & Spallarossa, D. (2025). Interevent variability in ground-motion prediction models: The role of the source parameter selection. *Bulletin of the Seismological Society of America, 115*, 2857–2866.

Bindi, D., Razafindrakoto, H. N. T., Picozzi, M., & Oth, A. (2021). Stress drop derived from spectral analysis considering the hypocentral depth in the attenuation model: Application to the Ridgecrest region, California. *Bulletin of the Seismological Society of America, 111*, 3175–3188.

Boore, D. M. (1983). Stochastic simulation of high-frequency ground motions based on seismological models of the radiated spectra. *Bulletin of the Seismological Society of America, 73*, 1865–1894.

Boore, D. M. (2003). Simulation of ground motion using the stochastic method, *Pure Appl. Geophys., 160*, 635–676.

Boore, D. M., & Joyner, W. B. (1997). Site amplifications for generic rock sites. *Bulletin of the Seismological Society of America, 87*, 327–341.

Brune, J. N. (1971). Correction. *Journal of Geophysical Research, 76*, 5002.

Castellaro, S., Alessandrini, G., & Musinu, G. (2022). Seismic station installations and their impact on the recorded signals and derived quantities. *Seismological Research Letters, 93*, 3348–3362.

Electric Power Research Institute (1993). Guidelines for determining design basis ground motions, Volume 2: Appendices for ground motion estimation. EPRI TR-102293. Final Rept.

Eshelby, J. D. (1957). The determination of the elastic field of an ellipsoidal inclusion, and related problems. *Proceedings of the Royal Society London, Series A, 241*, 376–396.

Gallovič, F., & Brokešová, J. (2004). On strong ground motion synthesis with k^{-2} slip distributions. *Journal of Seismology, 8*, 211–224.

Goulet, C. A., Kishida, T., Ancheta, T. D., Cramer, C. H., Darragh, R. B., Silva, W. J., Hashash, Y. M. A., Harmon, J., Parker, G. A., Stewart, J. P., & Youngs, R. R. (2021). PEER NGA-East Database. *Earthquake Spectra, 37*(S1), 1331–1353.

Graves, R. W., & Pitarka, A. (2010). Broadband ground-motion simulation using a hybrid approach. *Bulletin of the Seismological Society of America, 100*, 2095–2123.

Haendel, A., Pilz, M., & Cotton, F. (2023). Hard-rock κ_0 at KiK-net sites in Japan. *Bulletin of the Seismological Society of America, 113*, 2650–2665.

Hartzell, S. H., & Heaton, T. H. (1983). Inversion of strong ground motion and teleseismic waveform data for the fault rupture history of the 1979 Imperial Valley, California, earthquake. *Bulletin of the Seismological Society of America, 73*, 1553–1583.

Hartzell, S., & Helmberger, D. V. (1982). Strong-motion modeling of the Imperial Valley earthquake of 1979. *Bulletin of the Seismological Society of America, 72*, 571–596.

Heaton, T. H. (1982). The 1971 San Fernando earthquake: A double event? *Bulletin of the Seismological Society of America, 72*, 2037–2062.

Herrero, A., & Bernard, P. (1994). A kinematic self-similar rupture process for earthquakes. *Bulletin of the Seismological Society of America, 84*, 1216–1228.

Hollender, F., Roumelioti, Z., Maufroy, E., Traversa, P., & Mariscal, A. (2020). Can we trust high-frequency content in strong-motion database signals? Impact of housing, coupling, and installation depth of seismic sensors. *Seismological Research Letters, 91*, 2192–2205.

Infantino, M., Mazzieri, I., Ozcebe, A. G., Paolucci, R., & Stupazzini, M. (2020). 3D physics-based numerical simulations of ground motion in Istanbul from earthquakes along the Marmara segment of the North Anatolian fault. *Bulletin of the Seismological Society of America, 110*, 2559–2576.

Ji, C., Wald, D. J., & Helmberger, D. V. (2002). Source description of the 1999 Hector Mine, California, earthquake, Part I: Wavelet domain inversion theory and resolution analysis. *Bulletin of the Seismological Society of America, 92*, 1192–1207.

Kanamori, H., & Anderson, D. L. (1975). Theoretical basis of some empirical relations in seismology. *Bulletin of the Seismological Society of America, 65*, 1073–1095.

Kaneko, Y., & Shearer, P. M. (2014). Variability of seismic source spectra, estimated stress drop, and radiated energy, derived from cohesive-zone models of symmetrical and asymmetrical circular and elliptical ruptures. *Journal of Geophysical Research, 120*, 1053–1079.

Koper, K. D., Burlacu, R., Murray, R., Baker, B., Tibi, R., & Mueen, A. (2024). Inferring the focal depths of small earthquakes in southern California using physics-based waveform features. *Bulletin of the Seismological Society of America, 114*, 2376–2396.

Ktenidou, O.-J., Cotton, F., Abrahamson, N. A., & Anderson, J. G. (2014). Taxonomy of κ: A review of definitions and estimation approaches targeted to applications. *Seismological Research Letters, 85*, 135–146.

Kurzon, I., Lyakhovsky, V., & Sagy, A. (2025). New formulation reduces the scatter of earthquake stress-drop estimation. *Seismological Research Letters, 96*, 1989–1998.

Madariaga, R. (1977). High-frequency radiation from crack (stress drop) models of earthquake faulting. *Geophysical Journal of the Royal Astronomical Society, 51*, 625–651.

Madariaga, R. (1983). High frequency radiation from dynamic earthquake fault models. *Annales Geophysicae, 1*, 17–23.

Mai, P. M., & Beroza, G. C. (2002). A spatial random field model to characterize complexity in earthquake slip. *Journal of Geophysical Research, 107*, 2308.

Mai, P. M., Schorlemmer, D., Page, M., Ampuero, J.-P., Asano, K., Causse, M., Custodio, S., Fan, W., Festa, G., Galis, M., Gallovic, F., Imperatori, W., Käser, M., Malytskyy, D., Okuwaki, R., Pollitz, F., Passone, L., Razafindrakoto, H. N. T., Sekiguchi, H., … Zielke, O. (2016). The earthquake-source inversion validation (SIV) project. *Seismological Research Letters, 87*, 690–708.

Mendoza, C., Hartzell, S., Ramirez-Guzman, L., & Martinez-Lopez, R. (2024). Prediction of regional broadband strong ground motions using a teleseismic source model of the 18 April 2014 M_w 7.3 Papanoa, Mexico, earthquake. *Bulletin of the Seismological Society of America, 114*, 2524–2545.

Nye, T., Sahakian, V. J., King, E., Baltay, A., & Klimasewski, A. (2023). Estimates of κ_0 and effects on ground motions in the San Francisco Bay area. *Bulletin of the Seismological Society of America, 113*, 823–842.

Palmer, S. M., & Atkinson, G. M. (2023). Uncertainties in broadband determination of the high-frequency spectral decay, kappa, in eastern Canada. *Bulletin of the Seismological Society of America, 113*, 2666–2688.

Parolai, S. (2018). κ_0: Origin and usability. *Bulletin of the Seismological Society of America, 108*, 3446–3456.

Parolai, S. (2023). Direct estimation of the source corner frequency of minor to moderate earthquakes from Fourier phase spectra fitting. *Bulletin of the Seismological Society of America, 114*, 2310–2324.

Parolai, S., & Bindi, D. (2004). Influence of soil-layer properties on k evaluation. *Bulletin of the Seismological Society of America, 94*, 349–356.

Rodgers, A. J., Pitarka, A., Pankajakshan, R., Sjogreen, B., & Petersson, N. A. (2020). Regional-scale 3D ground-motion simulations of M_w 7 earthquakes on the Hayward fault, northern California resolving frequencies 0–10 Hz and including site-

response corrections. *Bulletin of the Seismological Society of America, 110*, 2862–2881.

Schmedes, J., Archuleta, R. J., & Lavallée, D. (2013). A kinematic rupture model generator incorporating spatial interdependency of earthquake source parameters. *Geophysical Journal International, 192*, 1116–1131.

Shearer, P. M. (2019). *Introduction to Seismology* (3rd ed.). Cambridge University Press: Cambridge.

Shi, Z., & Day, S. M. (2013). Rupture dynamics and ground motion from 3-D rough-fault simulations. *Journal of Geophysical Research, 118*, 1122–1141.

Somerville, P., Irikura, K., Graves, R., Sawada, S., Wald, D., Abrahamson, N., Iwasaki, Y., Kagawa, T., Smith, N., & Kowada, A. (1999). Characterizing crustal earthquake slip models for the prediction of strong ground motion. *Seismological Research Letters, 70*, 59–80.

Stewart, J. (1999). *Calculus* (4th ed.). Brooks/Cole Publishing Company.

Toro, G. R., Abrahamson, N. A., & Schneider, J. F. (1997). Model of strong ground motions from earthquakes in central and eastern North America: Best estimates and uncertainties. *Seismological Research Letters, 68*, 41–57.

Van Dyke, M. (1964). *Perturbation Methods in Fluid Mechanics*. Academic Press.

Wald, D. J., & Heaton, T. H. (1994). Spatial and temporal distribution of slip for the 1992 Landers, California, earthquake. *Bulletin of the Seismological Society of America, 84*, 668–691.

Ye, L., Lay, T., Kanamori, H., & Rivera, L. (2016). Rupture characteristics of major and great ($M_w \geq 7$) megathrust earthquakes from 1990 to 2015: 1. Source parameter scaling relationships. *Journal of Geophysical Research, 121*, 826–844.

Zuo, K., Zhao, C., & Kuang, W. (2025). SourceNet: A deep-learning-based method for determining earthquake source parameters. *Bulletin of the Seismological Society of America, 115*, 379–392.

(Received March 25, 2025, revised January 24, 2026, accepted January 30, 2026, Published online March 25, 2026)